

# Bi-plane correlation imaging for improved detection of lung nodules

Ehsan Samei<sup>1,2,3</sup>, David M. Catarious, Jr.<sup>1,2</sup>, Alan H. Baydush<sup>1,2,4</sup>  
Carey E. Floyd, Jr.<sup>1,2</sup>, Rene Vargas-Voracek<sup>1</sup>

<sup>1</sup>Department of Radiology, <sup>2</sup>Department of Biomedical Engineering  
<sup>3</sup>Department of Physics, <sup>4</sup>Department of Radiation Oncology  
Duke University, Durham, NC 27710

## ABSTRACT

Bi-plane correlation imaging (BCI) is a new imaging approach that utilizes angular information from a bi-plane digital acquisition in conjunction with computer assisted detection (CAD) to reduce the degrading influence of anatomical noise in the detection of subtle lesions in planar images. An anthropomorphic chest phantom, supplemented with added nodule phantoms (5-13 mm at the image plane), was imaged from different posterior projections within a  $\pm 12^\circ$  range by moving the x-ray tube vertically and horizontally with respect to the detector. Each image was analyzed using a basic front-end single-view CAD algorithm. The correlation of the suspect lesions from the PA view with those from each of the oblique views was examined using *a priori* knowledge of the acquisition geometry. The correlated suspect lesions were registered as positive. Using an optimum  $-3^\circ$  vertical geometry and processing parameters, BCI resulted in 62.5% sensitivity, 1.5 FP/image, and 0.885 PPV. The corresponding values from the observer experiment were 56% sensitivity, 10.8 FP/image, and 0.45 PPV, respectively. Compared to single-view CAD results, the BCI reduced sensitivity by 20%. However, the corresponding reduction in FPs was notably higher (94%) leading to 140% improvement in the PPV. Changes in processing parameters could result in higher PPV and lower FP/image at the expense of lower sensitivity. Similar findings were indicated for small (5-9 mm) and large (9-13 mm) nodules, but the relative improvement was significantly higher for smaller nodules. (The research was supported by a grant from the NIH, R21CA91806.)

**Keywords:** Chest radiography, digital radiography, stereoscopy, lung nodules, lung cancer, computer aided detection (CAD)

## 1. INTRODUCTION

Lung cancer is a leading cause of death in the US, surpassing the mortality associated with breast, prostate, colon, and cervical cancers combined (ACS 2002). In its early stages, lung cancer is often discovered in the form of solitary lung nodules when a chest radiograph of a patient is taken for another purpose. Many studies suggest that the probability of localized disease, and thus patient survival, is inversely proportional to the size of a nodule at the time of diagnosis (Padilla 1997, Mori 1989). Therefore, any improvement in the poor prognosis of lung cancer relies on improving the early detection of associated lung nodules when they are still small, and thus the probability of the spread of the disease is still low. In chest radiographs, small cancerous nodules are difficult to detect. Even very experienced radiologists often miss subtle lung nodules that can be detected if the image is viewed retrospectively after the disease is confirmed (Heelan 1984). In spite of much technological advancement in chest radiography in the last four decades, there has been little or no improvement in the detection of small lung nodules (Revesz 1977, Muhm 1983, Heelan 1984, Gavelli 1998).

There are three main factors limiting the detection of subtle lung nodules and early diagnosis of lung cancer: nodule contrast to noise ratio (CNR), perceptual errors, and anatomical noise. The detection of lung nodules can be influenced by their low CNR. There have been significant advancements in radiologic technology, including the development of digital radiographic systems, that have led to significant improvements in the resolution, noise, and latitude characteristics of thoracic images leading to improved CNR of lung lesions. Perceptual errors, at both visual and cognitive levels, are the second obstacle contributing to the low detection rate of subtle lung nodules (Kundel 1978, Kundel 1975, Carmody 1980). Computer assisted diagnosis (CAD) algorithms have also been developed as a method to provide a complete search of the image data and thus minimize perceptual errors in the detection of lung nodules in chest radiographs (Giger 1988). The third and perhaps the most significant obstacle with detrimental effects on the detection of lung nodules in chest

radiographs is anatomical noise, the normal thoracic structures surrounding and overlaying a lesion masking its appearance (Burgess 1997, Samei 2000, Revesz 1974, Neitzel 1998).

Several promising methods have been developed to reduce the influence of anatomical noise in thoracic images. Two such techniques that aim to improve lung nodule detection by minimizing the appearance of ribs and other overlaying thoracic structures are dual-energy imaging (Stewart 1990, Kido 1995) and digital tomosynthesis (Zwicker 1997, Dobbins 1998). The former technique, with only two systems commercially available, is currently under clinical evaluation, while the latter awaits further development and clinical implementation. Computed tomography is probably the optimal modality for minimizing anatomical noise in chest imaging as it eliminates overlays of anatomical structures associated with projection imaging. There has been recent excitement over the use of low-dose CT for lung cancer screening (Henschke 1999). However, at the present, utilization of CT as a wide-spread screening method for the detection of subtle lung nodules is controversial because of associated economic (cost and technology availability), patient care (e.g., over-treatment), and epidemiological (e.g., patient dose) issues.

This study proposes a new image acquisition and processing approach, bi-plane correlation imaging (BCI), for improving the detection of subtle lung nodules. In this approach, two digital images of the thorax are acquired within a short time interval from two slightly different posterior projections (Fig. 1). The image data are then incorporated into an enhanced CAD algorithm in which nodules are detected by examining the geometrical correlation of the detected signals in the two views. The underlying hypothesis of the proposed approach is that the anatomical noise associated with normal anatomical features in the thorax is the main factor limiting the detection of subtle lung lesions. Angular information is used to minimize this limiting influence by identifying and positively reinforcing the nodule signals, which remain relatively constant against a variation in the background structure. This approach does not promise to completely eliminate anatomical noise (as CT does), but aims to cost-effectively reduce its influence without an increase in the patient dose. Using correlation of signals between two views to identify “true” signals, CAD can be utilized at high sensitivity levels, lowering the detection thresholds, without an undesirable increase in the number of false positives. The hybrid approach of utilizing angular information in conjunction with digital acquisition and CAD addresses all three major obstacles to the detection of subtle lung nodules discussed above. The angular information reduces the effects of anatomical noise, the high signal-to-noise ratio of digital acquisition assures sufficient nodule contrast, and CAD incorporates a complete search. This paper reports on a study aimed to explore the feasibility of BCI for improved early detection of subtle lung nodules via a phantom experiment.

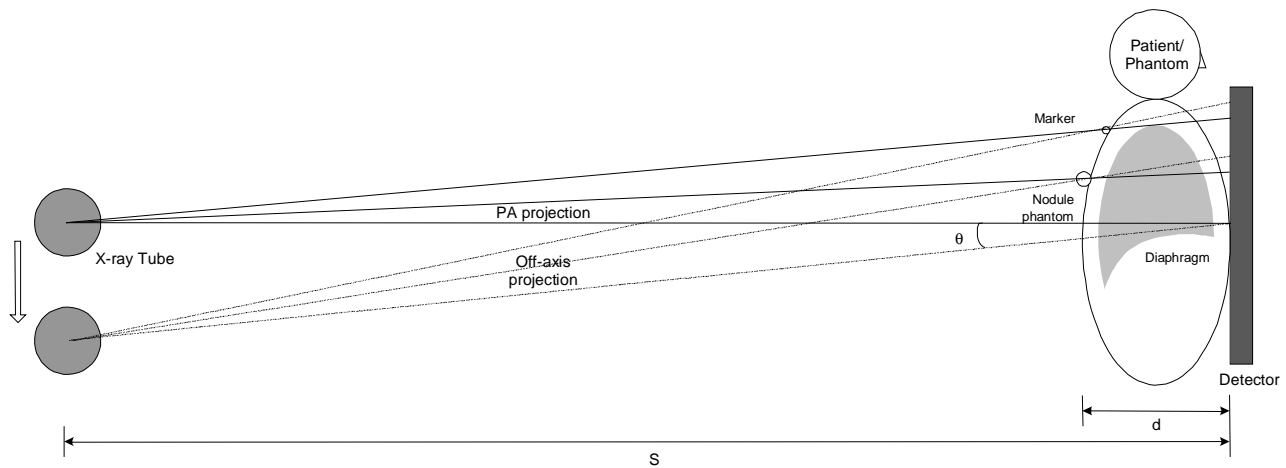


Fig. 1: The schematic geometry for the acquisition of BCI bi-plane image pairs at 0 (PA) and  $-6$  degrees

## 2. MATERIALS AND METHODS

### 1. Image acquisition

This study was performed based on images acquired from an anthropomorphic chest phantom (RSD, Inc., Long Beach, CA). The phantom was superimposed with 16 additional nodule phantoms of 8 different sizes made of Teflon emulating the appearance of subtle tissue-equivalent lesions in chest radiographs (4-11 mm in diameter) with a physical density within a 0.95-1.1 g/cm<sup>3</sup> range (Samei 1997). Table 1 lists the diameter, thickness, and contrast characteristics of the nodule phantoms. As the nodule phantoms were placed on the back of the chest phantom in PA acquisition geometry, they were magnified by about 20% to 5-13 mm in diameter. Four small fiducial markers were also added at four corners of the phantom for verifying the acquisition geometry. The supplemented phantom was imaged using a conventional PA geometry with a flat-panel digital radiographic system (GE, XQ/i). The exact locations of the nodules were recorded via an additional image with the locations of the nodules marked with fiducial markers (Fig. 2).

In addition to the PA view, by vertically adjusting the x-ray tube, the supplemented phantom was imaged using seven additional projection orientations at -6°, -4°, -3°, +3°, +4°, +6°, and +12° (Fig. 1). The x-ray tube was moved between these angular positions using a precise programmable tube mover (Fig. 3). The above acquisitions were repeated with the 16 nodule phantoms placed in a different arrangement configuration to allow superimposition of a given nodule against various local anatomical backgrounds. A conventional kVp (120) and standard photo-timed exposure (mAs = 5) were used for the acquisitions. The acquisitions were repeated with the supplemented phantom rotated 90 degrees to assess the utility of BCI with horizontal (i.e. lateral) displacement of the x-ray tube in the two projections. The images were corrected for offset and gain non-uniformities without any additional image processing. The total of 32 projection images (8 projections x 2 nodule configurations x 2 orientations) were stored electronically.

Table 1 illustrates the realization of the nodule phantoms in one of the PA radiographs. As evident in the illustration, the lesions were extremely subtle and most of them were below the size considered the threshold of detectability, 10 cm, on chest radiographs, 10 mm (Kundel 1981).

All the acquired oblique images were paired with a corresponding 0 degree/ PA image to be used for determining the optimum acquisition geometry as described below. In the acquired image set, the relative angular separation of any oblique view from the corresponding PA view was verified by correlating the coordinates of the four fixed fiducial markers placed at the corners of the image area. The results showed excellent geometrical accuracy, with sub-mm precision for geometrical correlation of anatomical features. For each image, a truth file was also generated from the known location of the nodule phantoms to be used for evaluating the performance of the CAD algorithm described below.

*Table 1: The characteristics of the nodule phantoms. The diameters were 20% higher in the imaging plane because of magnification. The estimated peak contrasts were determined from the maximum thickness of the phantoms, an assumed scatter-to-primary ratio of 0.68, and an effective linear attenuation coefficient of 0.045126 mm<sup>-1</sup> as defined in Samei et al. (Samei 1997) and estimated for a 0.5 mm thick CsI detector using the xSpect x-ray simulation routine.*

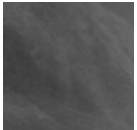
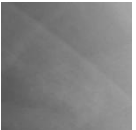
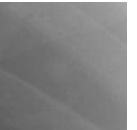
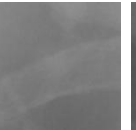
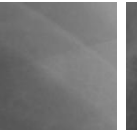
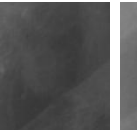
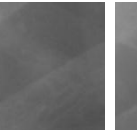

Diameter (mm)	3.9	5.5	5.0	7.8	7.0	9.3	8.4	11.0
Maximum thickness (mm)	1.52	2.12	2.36	3.00	3.35	3.56	3.95	4.27
Estimated peak contrast, dE/E (%)	4.1	5.7	6.3	8.1	9.0	9.6	10.6	11.5
Emulated peak physical density (g/cm <sup>3</sup> )	0.95	0.95	1.1	0.95	1.1	0.95	1.1	0.95
Nodule appearance								



Fig. 2: A PA chest image with the location of the added the nodules marked with fiducial markers



Fig. 3: The tube mover used to acquire bi-plane data.

## 2. Single-view CAD

A single-view CAD algorithm has been under development at our research laboratory. The acquired phantom images were processed by the algorithm and the results were used as input to the BCI scheme described in the next section.

The CAD algorithm consisted of four stages: A) image preprocessing, B) filtration, C) suspicious region localization, D) feature extraction, and D) classification/false positive reduction. At the image preprocessing stage, the images were first inverted and then converted to a logarithmic scale. The lung fields were segmented via hand-drawn outlines, a segmentation step expected to be automated in the next version of the algorithm. The image preprocessing stage also included a background regularization process via unsharp-masking (USM) or local histogram equalization (LHE) (Gonzalez 1993). USM suppresses low-frequency background information while emphasizing the high-frequency content of an image. Subtracting a low-pass filtered version of the original image enhances the high-frequency content and corrects for non-uniformities in the background, therefore potentially raising the detectability of the nodules. Alternatively, LHE is able to accentuate local details while preserving the overall, or low-frequency, structure of the image, leading to increased local contrast. The USM processing was applied according to  $I(x,y) = A.O(x,y) - L[O(x,y)]$ , where  $I(x,y)$  is the new image,  $O(x,y)$  is the original image,  $A$  is a scalar in  $[0, 1]$ , and  $L$  is a low-pass rectangular average filtering operator. In the LHE process, each pixel in the original image was transformed into a new pixel by  $I(x,y) = A(x,y).[O(x,y) - m(x,y)] + m(x,y)$ , where  $A(x,y) = kM/\sigma(x,y)$ ,  $M$  represents the global mean of the image,  $k$  is a scalar in  $[0, 1]$ , and  $\sigma(x,y)$  and  $m(x,y)$  are the local standard deviation and local mean of pixels in a kernel/window around  $(x, y)$ . In this study, the kernel sizes for this operator were varied between 28 and 52 mm for a fixed  $A = k = 0.5$ .

After pre-processing, the images were filtered for enhancing nodule-like features within the images. Since it has been demonstrated that lung nodules generally follow a Gaussian-like profile (Samei 1997), a Difference Of Gaussian (DOG) filter was used (Zheng 1995). Two DOG filters were utilized with two different combinations of the standard deviation widths of the two defining Gaussian components, 8/4 or 8/2 mm. These particular combinations were selected based on an iterative empirical approach for best performance. The kernel size of the DOG and the kernel size of the preprocessor were always chosen to be equal. The DOG filter was applied using the normalized cross-correlation (NCC) method (Gonzalez 1993, Carreira 1998, Penedo 1998). Unlike conventional cross-correlation, NCC is amplitude independent, and thus

suitable to the widely varying background of chest images. The output of the filtration was an image with values ranging between  $-1$  and  $+1$ , with the extremes corresponding to the perfect mismatch or match of the original image to the targeted DOG profile, respectively.

The filtered images were further processed to identify suspicious nodule locations via a multi-level thresholding procedure. In this procedure, regions were identified at eleven gray level thresholds. As the threshold levels progress, some of the regions would grow and merge with their neighbors. The final set of suspicious regions was determined by extracting the suspicious regions at the threshold level before they merged with another region.

Finally, from each of the suspicious regions, twelve features were extracted. These features included area, eccentricity, major axis length, minor axis length, convex area (the area of the convex hull), equivalent diameter (diameter of the circle that has an area equal to that of the region), orientation, the filled region (the area of the region including internal voids), Euler number (the number of objects in the region minus the number of holes in those objects), solidity (the area of the region divided by area of the convex hull), and extent (the area of the region divided by area of the bounding box - smallest enclosing rectangle). To classify the suspicious regions as being nodules or nonnodules, a multistep linear classifier was employed. Specifically, each pair of extracted features was combined via Fisher's linear discriminant (Nadler 1993), and classification decisions were made. The thresholds on the classification outputs were empirically determined so as to minimize the number of true positives eliminated. Once each pair of features was compared and classification decisions were made, all decisions were logically "ANDed" to make the final classification decision. Round-robin training and testing was employed in the classification procedure.

The ground truth was specified by binary images that indicated the location and sizes of the true lesions in the images. A nodule was counted as being "hit" when any part of the suspicious region fell within 5 mm of the centroid of the true lesion.

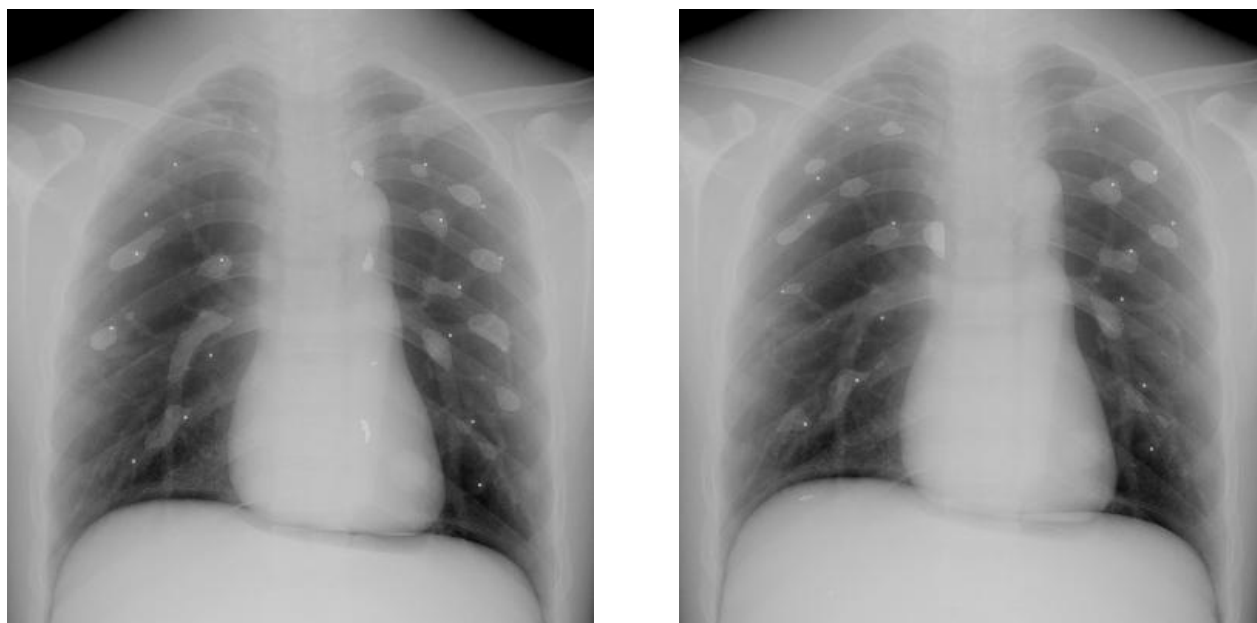


*Fig. 4: A PA (left) and  $-3^\circ$  oblique (right) radiograph of the chest phantom. The fiducial markers mark the center of true lesions, while the bright areas are suspect lesions identified by single-view. In single-view CAD, a TP is registered if any area of the CAD "island" is within a 5 mm radius of the true lesion. In the BCI scheme, a TP is registered when a TP in the PA view coincides/correlates with a suspect lesion in the oblique view based on the known angular separation of the two views. If a FP in the PA view correlates with a suspect lesion (true or false) in the other view, the suspect lesion is considered a FP in the BCI scheme.*

### 3. BCI detection scheme

The single-view CAD algorithm described above was supplemented with a bi-plane correlation routine. In BCI, the geometrical correlation of the detected signals in the two views of a bi-plane image pair data is examined in order to detect subtle lung nodules with a high-sensitivity while minimizing the number of false-positives by applying a geometrical correlation rule. In the routine, the PA image was used as the reference image. For each suspected region in the PA image, the known angular separation between the PA and an oblique image was used to locate the possible location where the geometrically-shifted image of the candidate nodule might be expected to appear in the oblique view depending on nodule's location within the thoracic cavity (Fig. 4).

To take into account the shift in the location of the suspect regions due to overlapping thoracic structure, a margin parameter defined a degree of tolerance from the perfect geometrical correlation between the two views in the horizontal and vertical directions. The resultant rectangular mask had a width equal to twice the margin size, and a length equal to maximum possible displacement based on angular separation plus the margin size. If a suspect region was identified within the mask, the original suspect region in the PA view was scored as positive. If more than one suspect region was found within the mask, only one of them was counted. A true-positive was indicated when a correlated suspect region pair corresponded to a true-positive in the PA view. Otherwise the correlated pair was registered as false-positive.

Additional correlation rules were also applied based on the closeness in the area and the eccentricity of suspect lesion pairs calculated from an area correlation index or an eccentricity correlation index defined as  $2|A_{PA}-A_{obl}|/(A_{PA}+A_{obl})$  or  $2|X_{PA}-X_{obl}|/(X_{PA}+X_{obl})$  where A and X are the area and eccentricity, respectively. A pair of suspect lesions was registered as FP if their associated indices fell outside of specific thresholds.

Table 2: Performance of the single-view CAD as a function of processing parameters averaged over all the acquired images.

DOG filter size	Pre-processing method	Preprocessing kernel size, mm	Sensitivity (%)	FP	PPV
8/4 mm	None	28	76.76	100.4	0.109
		36	74.22	56.0	0.175
		44	72.46	32.1	0.266
	LHE	28	84.57	20.3	0.400
		36	80.08	23.7	0.351
		44	77.15	23.4	0.345
	USM	28	84.18	64.6	0.172
		36	78.71	38.0	0.249
		44	75.78	20.2	0.375
8/2 mm	None	28	85.55	117.9	0.104
		36	82.03	80.4	0.140
		44	81.64	56.4	0.188
	LHE	28	90.82	48.6	0.230
		36	88.48	40.2	0.261
		44	84.96	36.7	0.271
	USM	28	90.62	85.2	0.145
		36	86.13	69.1	0.166
		44	83.98	52.1	0.205

### 4. BCI evaluation

The acquired phantom images were processed using the CAD and BCI processing schemes described above. Each oblique view projection image was paired with its corresponding PA radiograph. The results were analyzed to find the best processing and acquisition parameters for optimum performance. The independent parameters were the following:

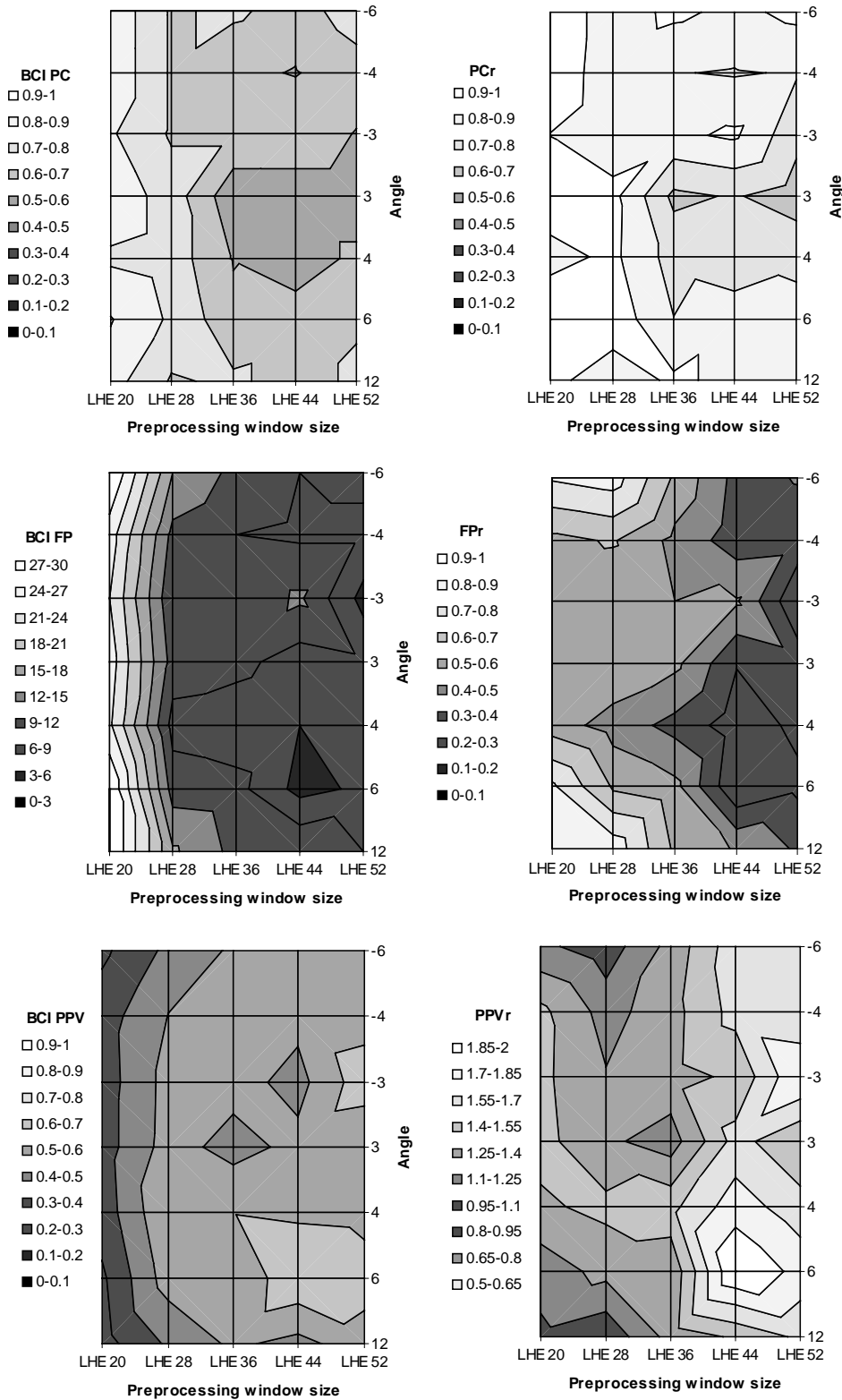


Fig. 5: Variation in percent correct (sensitivity), false positive rate, and PPV of BCI (left column) and of BCI compared to single-view CAD (BCI/CAD ratio, right column) as a function of vertical displacement angle and pre-processing kernel size (LHE pre-processing, 8/4 mm DOG) (no area or eccentricity correlation rule).

1. Angular separation (-6 to 12 degrees)
2. Displacement orientation (horizontal and vertical)
3. CAD pre-processing method (USM, LHE, and none)
4. CAD pre-processing and DOG kernel size (28, 36, 44, and 52 mm)
5. Standard deviations of the DOG filter (8/4 mm and 8/2 mm)
6. Correlation margin size (2-10 mm)
7. Area correlation index (0-2)
8. Eccentricity correlation index (0-2)

The optimization/evaluation of these parameters was performed based on six figures of merit:

1. Percent correct (PC) when using BCI as the ratio of true positives to true positives plus false negatives
2. False positives per image (FP) when using BCI
3. Positive predictive value (PPV) when using BCI
4. The relative improvement of the PC when using BCI relative to single-view CAD (PCr)
5. The relative improvement of the FP when using BCI relative to single-view CAD (FPr)
6. The relative improvement of the PPV when using BCI relative to single-view CAD (PPVr)

In order to identify the optimum set of processing parameters, the figure of merit

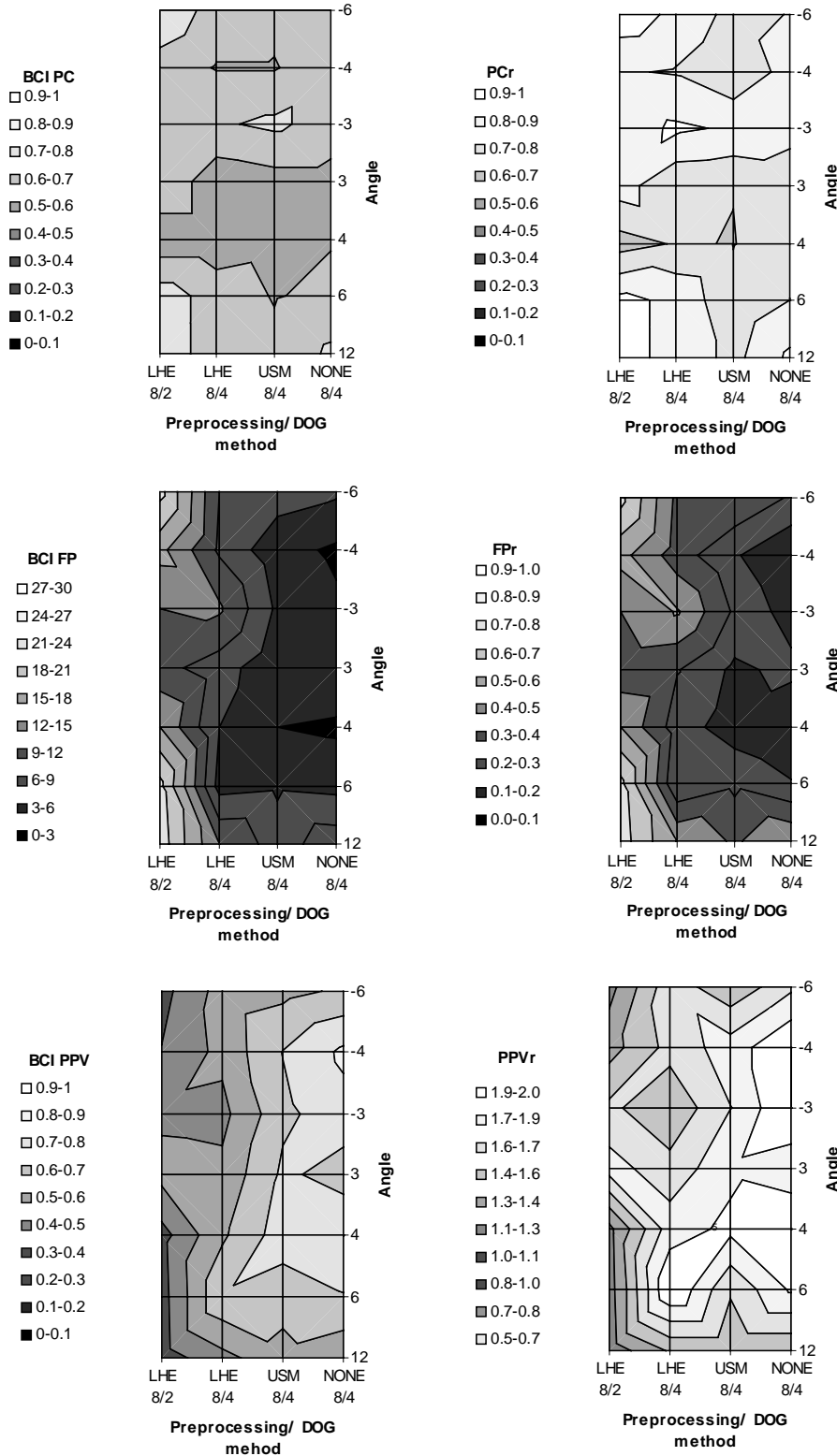


Fig. 6: Variation in percent correct (sensitivity), false positive rate, and PPV of BCI (left column) and of BCI compared to single-view CAD (BCI/CAD ratio, right column) as a function of vertical displacement angle and pre-processing method (fixed 44 mm kernel size) and DOG filter size (8/2 and 8/4 mm) (no area or eccentricity correlation rule).

results were initially scanned for optima across the ranges of influencing processing variables, identifying initial parameter values that yield the best results. Fixing the variables at those specific values, the figures of merit were then examined at each acquisition angle across each single variable. The values of the fixed parameters were then iteratively changed until the optimum parameter combinations were found.

In addition to the computer analysis of the images, the 16 vertical displacement images were read by an experienced chest radiologist who was asked to identify any suspect extremely subtle lesions in the images. The performance of the radiologist was used as a benchmark for the subtlety of the lesions. The observer's PC, FP, and PPV, averaged over all 16 images, were compared to the corresponding figures from the BCI and from the single-view CAD to assess the relative merit of BCI and the advantage of utilizing image data from a second view.

### 3. RESULTS

The single-view CAD showed notable variability as a function of processing parameter. The sensitivity, false positive, and positive predictive figures, averaged over all images, are listed in Table 2. There was a general tradeoff between sensitivity and false positives, as parameters leading to higher sensitivity also generated a larger number of false positives. The best combination of parameters (8/4

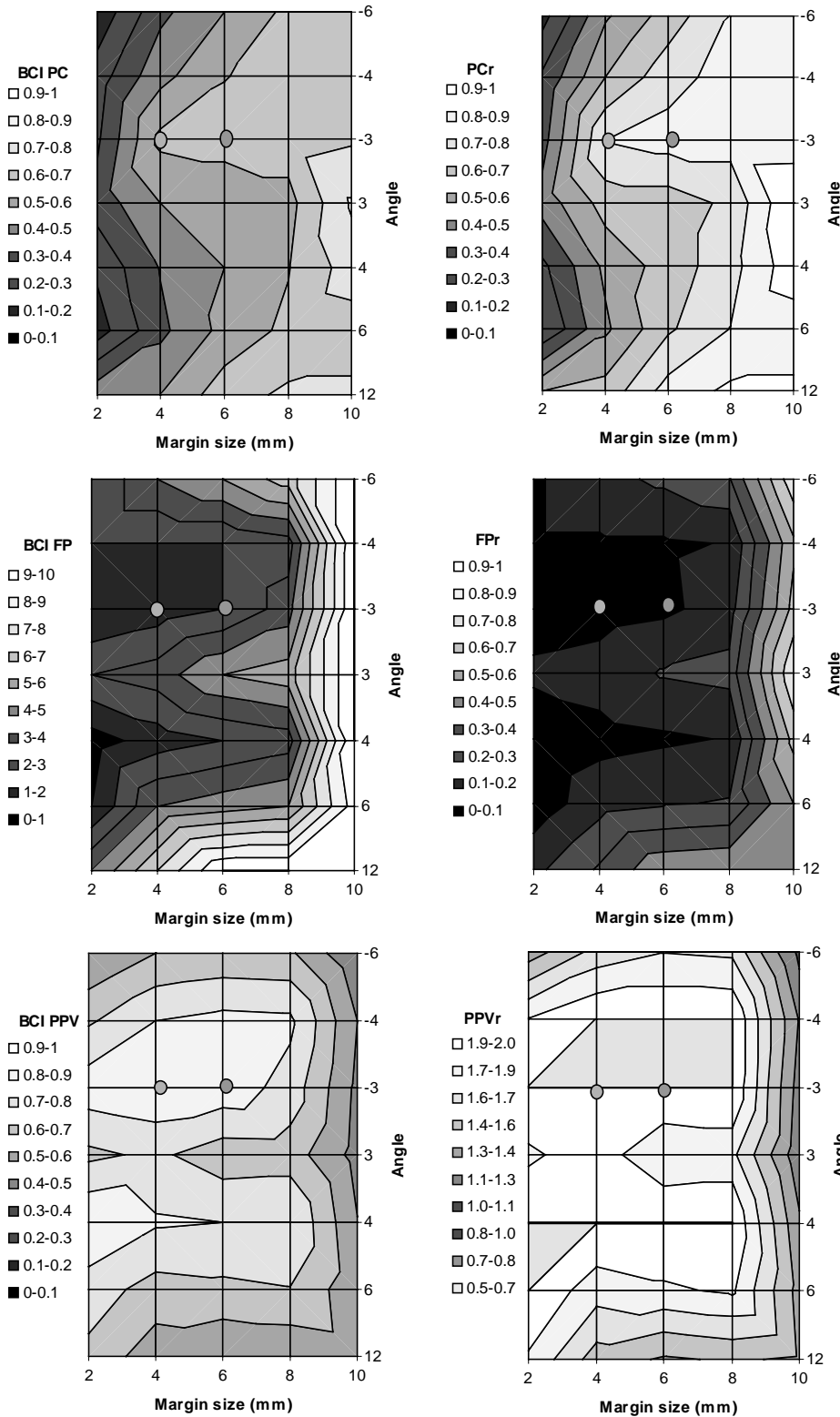


Fig. 7: Variation in percent correct (sensitivity), false positive rate, and PPV of BCI (left column) and of BCI compared to single-view CAD (BCI/CAD ratio, right column) as a function of vertical displacement angle and correlation area margin in mm (no pre-processing, 44 mm kernel size, 8/4 DOG, no area or eccentricity correlation rule). Optimal parameters are marked with two circles.

mm DOG, LHE, 28 mm) provided 85% sensitivity at 20 false-positives per image for a PPV of 0.4. Clearly this level of performance is insufficient for a conventional clinical CAD implementation. This performance, however, exceeds what is expected from a single-view CAD algorithm without more sophisticated false-positive reduction strategies, given the subtlety of the lesions under consideration. Furthermore, operating at a high sensitivity/FP region, the BCI scheme was specifically designed to reduce the number of false-positives via its geometrical correlation rule. Nevertheless, research is in progress to further improve the performance of our single-view CAD with additional false-positive reduction methods.

Even though some of the processing parameters combinations exhibited better performance in single-view CAD processes, it was unclear which ones might yield optimum BCI performance. Thus all the combinations of CAD processing parameters were considered for the BCI processing. In terms of pre-processing, Fig. 5 illustrates the dependency of the BCI performance on the kernel size (for LHE pre-processing) at all the examined oblique acquisition angles. The results clearly indicate that the BCI scheme reduces the sensitivity and FP of the single-view CAD. However, the corresponding reduction in FPs is notably higher leading to an improvement in PPV, regardless of the kernel size and the acquisition angle. The results further suggest that a kernel size of 44 mm provides better overall performance in

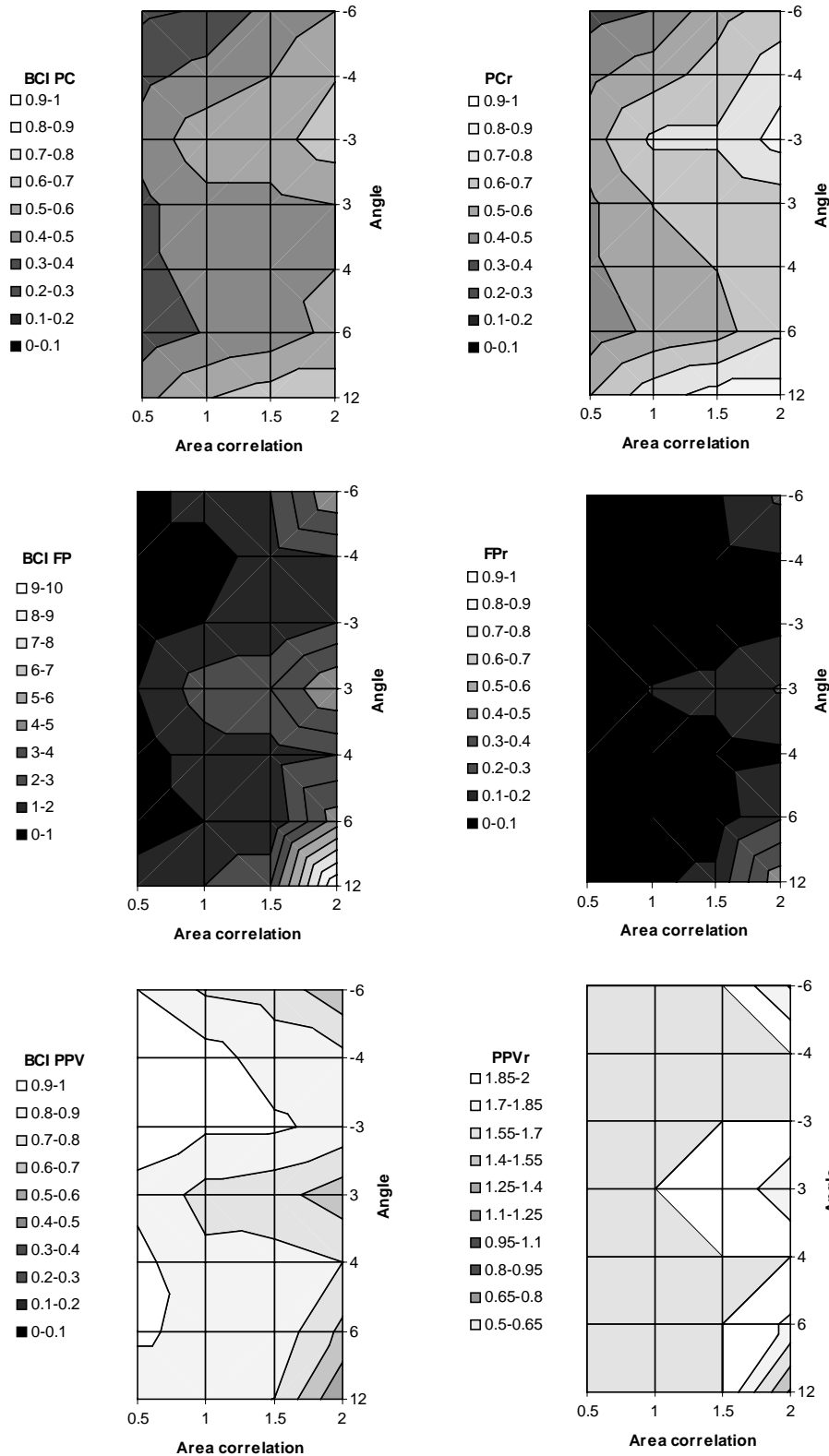


Fig. 8: Variation in percent correct (sensitivity), false positive rate, and PPV of BCI (left column) and of BCI compared to single-view CAD (BCI/CAD ratio, right column) as a function of vertical displacement angle and area correlation index (no pre-processing, 44 mm kernel size, 8/4 mm DOG, 6 mm correlation margin).

terms of the PPV and PPV improvement.

Fig. 6 similarly illustrates the BCI performance as a function of DOG filter size and pre-processing method for a fixed 44 mm kernel size. The results indicate that 8/4 mm DOG filter size provides better performance, a finding consistent with the single-view CAD results of Table 2. However, no pre-processing of the images proves to provide a better performance for the BCI method, as opposed to the LHE pre-processing, which was found optimum for single-view CAD (Table 2).

Basing the follow-up analysis on no pre-processing method, Fig. 7 illustrates the impact of the correlation margin size on performance. As the margin size increases from a restrictive 2 mm value, both sensitivity and the number of FPs increases. Aiming to maintain a sensitivity higher than 60%, optimum performance, in terms of both the BCI performance alone, and the relative improvement with respect to single-view CAD, is exhibited at a margin size of 4-6 mm at  $-3^\circ$  acquisition angle. Beyond 4-6 mm margin size, the number of false positives increases at a faster rate leading to a reduction in the PPV. The optimal regions are marked in the figure.

Basing the follow-up analysis on 6 mm correlation margin size, Fig. 8 illustrates the impact of imposing additional area correlation rule on the results. The results suggest that addition area correlation reduces both sensitivity and FPs with similar rate without causing any improvement in

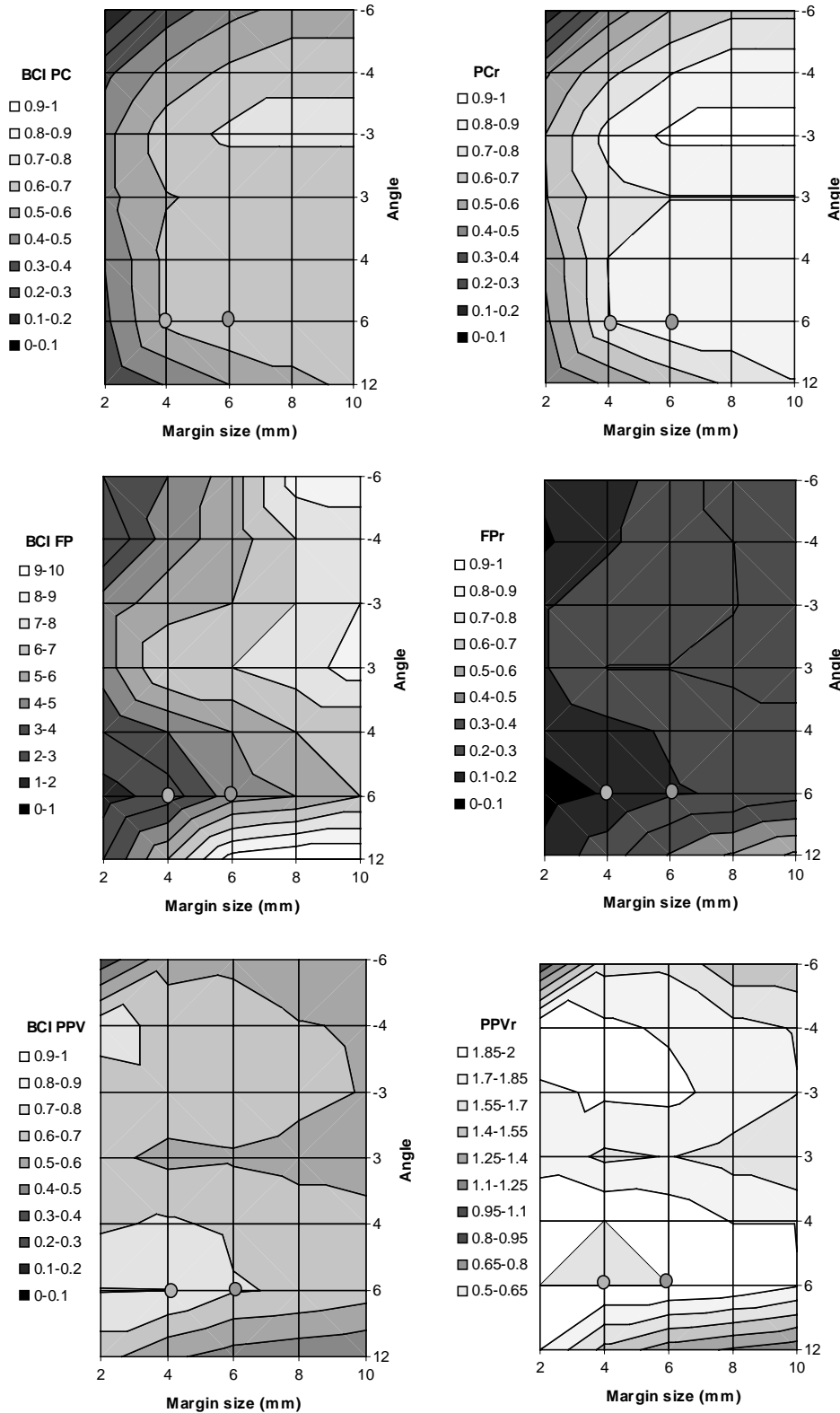


Fig. 9: Variation in percent correct (sensitivity), false positive rate, and PPV of BCI (left column) and of BCI compared to single-view CAD (BCI/CAD ratio, right column) as a function of horizontal displacement angle and correlation area margin in mm (USM pre-processing, 44 mm kernel size, 8/4 DOG, no area or eccentricity correlation rule). Optimal parameters are marked with two circles.

the PPV. Similar results were obtained when applying an addition eccentricity rule.

The results for horizontal displacement exhibited similar dependencies, except that the best performance was provided by USM processing (with 44 mm kernel size and 8/4 DOG). Fig. 9 illustrates the horizontal displacement results for this parameter combination as a function of correlation margin size and displacement angle. Again, aiming to maintain a sensitivity higher than 60%, optimum performance, in terms of both the BCI performance alone, and the relative improvement with respect to single-view CAD, was exhibited for a margin size of 4-6 mm at +6° acquisition angle. Similar to vertical displacement results, the horizontal results did not show any improvement in the PPV with the additional area or eccentricity correlation rules.

Taking into account all the dependencies described above, the optimum oblique view for the acquisition angle appeared to be at around -3° vertical displacement or +6° horizontal displacement, 8/4 mm DOG, 4-6 mm margin size, and no area or eccentricity correlations. Table 3 provides the actual figures of merit for the optimum performance of the BCI method. The summary results show that vertical displacement yields better results. Furthermore, breaking the lesions into small (4.7-8.7 mm) and large (8.7-13.3 mm) sizes indicate that the percent improvement compared to single-view CAD is higher for smaller lesions.

Using the optimum geometry ( $0/-3^\circ$  vertical displacement) and processing parameters, BCI results in 62.5% sensitivity, 1.5 FP/image, and 0.885 PPV. The corresponding values from the observer experiment were 56%, 10.8, and 0.45, respectively. Compared to single-view CAD results, the BCI reduced sensitivity by 20%. However, the corresponding reduction in FPs was notably higher (94%) leading to 140% improvement in the PPV. Adjustment in the processing parameters could yield higher sensitivity at the expense of higher FPs.

#### 4. DISCUSSION

Currently, no radiologic screening program exists for early detection of lung cancer. Early detection presently relies on chest radiography examinations performed on asymptomatic patients for other diagnostic purposes. There have been studies that favor using chest radiography as a screening tool (Shimizu 1992, Brett 1969). However, the usefulness of such a screening program for lung cancer has been questioned based upon its ineffectiveness either in diagnosis (Gurney 1995) or in changing the mortality rate once the cancer is diagnosed (Fontana 1991). If lung nodules could be reliably detected in earlier stages of lung cancer, a screening program could be justified. Apart from low-dose CT, which is currently under investigation, current radiologic technology is unable to either visually or computationally (i.e., using CAD) image/detect lung nodules at a sufficiently early stage without generating a large number of false positives. The percentage of false-positive diagnoses unfavorably affects the predictive value of a screening program, especially when the prevalence of the disease is low (Kundel 1981). CT can surpass many of the limitation of chest radiography in imaging lung cancer (Henschke 1999). However, its utilization as a screening method raises economical (cost and technology availability), patient care (e.g., over-treatment), and epidemiological (e.g., patient dose) issues.

BCI is a new imaging technique that has not been investigated in the past. The phantom-based findings reported in this paper, the first public report of the technique, suggest significant potential of BCI to surpass the fundamental anatomical noise limitations of chest radiographic imaging and chest CAD and to improve the early detection of subtle lung nodules. A more sensitive and specific diagnostic approach for smaller lesions (4-11 mm diameter unmagnified size in this study), BCI has the potential to change the current state of practice, perhaps leading to a preventive lung cancer screening program for high-risk populations. The cost associated with the technology is minimal, and thus it can be implemented cost-effectively at doses comparable to chest radiography.

These findings of this study require further important validations. An open issue is the sensitivity of the BCI performance to the initial performance level of the single-view CAD algorithm. We intend to test the BCI scheme using different CAD algorithms, algorithms with more aggressive FP reduction strategies, and an iteratively combined dual-view CAD scheme. In terms of acquisition, plans are underway to assess the sensitivity of the BCI performance to exposure, potentially reducing the total exposure to that of a single PA chest exam. Finally, the performance of the technique should be measured on human subjects with confirmed lung nodules, with additional strategies to minimize possible motion artifacts.

Table 3: The optimal performance of the BCI for lesions within various size ranges for vertical and horizontal displacement of the x-ray tube. The vertical displacement images were processed with no preprocessing, 44 mm kernel size, and 8/4 mm DOG. The horizontal displacement images were processed with USM pre-processing, 44 mm kernel size, and 8/4 mm DOG.

	0/-3° Vertical Displacement						0/+6° Horizontal Displacement					
	5-13 mm		5-9 mm		9-13 mm		5-13 mm		5-9 mm		9-13 mm	
Margin	4 mm	6 mm	4 mm	6 mm	4 mm	6 mm	4 mm	6 mm	4 mm	6 mm	4 mm	6 mm
BCI PC	62.5%	65.6%	62.5%	68.8%	62.5%	62.5%	62.5%	68.8%	68.8%	81.3%	56.3%	56.3%
BCI FP	1.5	2.0	1.5	2.0	1.5	2.0	2.5	4.5	2.5	4.5	2.5	4.5
BCI PPV	0.885	0.867	0.833	0.818	0.786	0.750	0.802	0.708	0.691	0.591	0.646	0.500
PCr	0.801	0.840	0.929	1.000	0.708	0.708	0.798	0.878	0.786	0.929	0.817	0.817
FPr	0.058	0.077	0.058	0.077	0.058	0.077	0.108	0.191	0.108	0.191	0.108	0.191
PPVr	2.404	2.350	4.322	4.250	3.149	2.959	2.319	2.038	3.014	2.565	3.459	2.630

## ACKNOWLEDGEMENTS

The authors wish to thank James Dobbins and Devon Godfrey for their assistance with this study in the use of the tube moving device.

## REFERENCES

1. American Cancer Society. Cancer facts and figures - 2002, Atlanta, GA, 2002.
2. G.Z. Brett. Earlier diagnosis and survival in lung cancer. *British Medical Journal*, 4:260-262, 1969.
3. A.E. Burgess, X. Li and C.K. Abbey. Nodule detection in two component noise: toward patient structure. Volume 3036 of *SPIE Medical Imaging*, pages 2-13, 1997.
4. D.P. Carmody, C.F. Nodine, and H.L. Kundel. An analysis of perceptual and cognitive factors in radiographic interpretation. *Perception*, 9:339-344, 1980.
5. M.J. Carreira, D. Cabello, et al. Computer-aided diagnoses: Automatic detection of lung nodules, *Med Phys* 25(10): 1998-2006, 1998.
6. J.T. Dobbins, R.L. Webber, and S.M. Hames. Thomosynthesis for improved pulmonary nodule detection. *Radiology*, 209(P):280, 1998.
7. R.S. Fontana, D.R. Sanderson, L.B. Woolner, W.F. Taylor, W.E. Miller, J.R. Muhm, P.E. Barnatz, W.S. Payne, P.C. Pairolero, and E.J. Bergstralh. Screening for lung cancer: a critique of the Mayo lung project. *Cancer*, 67:1155-1164, 1991.
8. G. Gavelli and E. Giampalma. Sensitivity and specificity of chest x-ray screening for lung cancer. Proceedings of the International Conference on Prevention and early Diagnosis of Lung Cancer, pages 103-108, 1998.
9. M.S. Giger, K. Doi, and H. MacMahon. Image feature analysis and computer-aided diagnosis in digital radiography, 3. Automated detection of nodules in peripheral lung fields. *Medical Physics*, 15(2):158-166, 1988.
10. R.C. Gonzalez, R.E. Woods, Digital Image Processing. New York, Addison-Wesley. 3rd ed., 1993.
11. J.W. Gurney. Why chest radiography became routine. *Radiology*, 195:245-246, 1995.
12. C.I. Henschke, D.I. McCauley, D.F. Yankelevitz, D.P. Naidich, G. McGuinness, et al., Early lung cancer action project: overall design and findings from baseline screening, *Lancet* 354: 99-105, 1999.
13. S. Kido, J. Ikezoe, H. Naito, J. Arisawa, S. Tamura, T. Kozuka, W. Ito and H. Kato. Clinical evaluation of pulmonary nodules with single-exposure dual-energy subtraction chest radiography with an iterative noise-reduction algorithm. *Radiology*, 194(2):407-412, 1995.
14. H.L. Kundel. Predictive value and threshold detectability of lung tumors. *Radiology*, 139:25-29. 1981.
15. H.L. Kundel, C.F. Nodine and D. Carmody. Visual scanning, pattern recognition and decision-making in pulmonary nodule detection. *Investigative Radiology*, 13:175-181, 1978.
16. H.L. Kundel and C.F. Nodine. Interpreting chest radiographs without visual search. *Radiology*, 116:527-532, 1975.
17. J. Padilla, V. Calvo, J.C. Penalver, G.Sales, and A. Morcillo. Surgical results and prognostic factors in early non-small cell lung cancer. *Annals of Thoracic Surgery*, 63(3):324-326, 1997.
18. R.T. Heelan, B.J. Flehinger, M.R. Melamed, M.B. Zaman and W.B. Perchick. Non-small-cell lung cancer: results of the New York screening program. *Radiology*, 151:289-293, 1984.
19. K. Mori, N. Yanase, M. Kaneko, R. Ono, and S. Ikeda. Diagnosis of peripheral lung cancer in cases of tumors 2 cm or less in size. *Chest*, 95:304-308, 1989.
20. J.R. Muhm, W.E. Miller, R.S. Fontana, D.R. Sanderson, and M.A. Uhlenhopp. Lung cancer detected during a screening program using four-month chest radiographs. *Radiology*, 148:561-565, 1983.
21. M. Nadler, E.P. Smith, Pattern Recognition Engineering. New York, New York, John Wiley and Sons, 1993.
22. U. Neitzel, T. Pralow, C. Schaefer-Prokop and M. Prokop. Influence of scatter reduction on lesion signal-to-noise ratio and lesion detection in digital chest radiography. volume 3336 of *SPIE Medical Imaging*, 1998.
23. M.G. Penedo, M.J. Carreira, et al. Computer-aided diagnosis: a neural-network-based approach to lung nodule detection, *IEEE Trans Med Imaging* 17(6): 872-80, 1998.
24. G. Revesz and H.L. Kundel. Psychophysical studies of detection errors in chest radiology. *Radiology*, 123:559-562, 1977.
25. G. Revesz, H.L. Kundel and M.A. Graber. The influence of structured noise on the detection of radiologic abnormalities. *Investigative Radiology*, 9:479-486, 1974.

26. E. Samei, W.R. Eyler, and L.F. Baron. Effects of Anatomical Structure on Signal Detection. *Handbook of Medical Imaging, Vol. 1 Physics and Psychophysics*. Eds. J. Beutel, R. Van Metter, and H. Kundel. SPIE Press, Bellingham, WA, 2000.
27. E. Samei, M.J. Flynn, W. Eyler, Simulation of subtle lung nodules in projection chest radiography, *Radiology* 202(1): 117-124, 1997.
28. N. Shimizu, A. Ando, S. Teramoto, Y. Moritani, and K. Nishii. Outcome of patients with lung cancer detected via mass screening as compared to those presented with symptoms. *J Surgical Oncology*, 50(1):7-11, 1992.
29. B.K. Stewart and H.K. Huang. Single-exposure dual-energy computed radiography. *Method Physics*, 17(5):866-875, 1990.
30. B. Zheng, Y.H. Chang, et al. Computerized detection of masses in digitized mammograms using single-image segmentation and a multilayer topographic feature analysis." *Academic Radiology* 2(11): 959-966, 1995.
31. R.D. Zwicker and N.A. Atari, Transverse tomosynthesis on a digital simulator. *Medical Physics*, 24(6):867-71, 1997.